

# *Ab initio* Identification of Hydrogen Tunneling as Two-Level Systems in Nb<sub>2</sub>O<sub>5</sub> and Ta<sub>2</sub>O<sub>5</sub>

Cristóbal Méndez<sup>1</sup> and Tomás A. Arias<sup>2</sup>

<sup>1</sup>*School of Applied and Engineering Physics, Cornell University, Ithaca, NY, 14853*

<sup>2</sup>*Department of Physics, Cornell University, Ithaca, New York 14853*

(Dated: March 19, 2026)

Two-level systems (TLS) in native Nb and Ta oxides limit superconducting-qubit coherence and SRF-cavity quality factors in the microwave frequency range, yet their microscopic origin remains unclear. We combine MLIP-accelerated sampling of hydrogen configurations and diffusion pathways in amorphous Nb and Ta pentoxides with targeted *ab initio* validation. Hydrogen is the only light interstitial with barrier–distance combinations near the  $\sim 0.1 - 10$  GHz tunneling regime, and its ensemble statistics in amorphous oxides produce effective TLS densities and loss estimates consistent with the experimentally observed higher loss in Nb oxide than in Ta oxide. Our results point to H tunneling as a plausible microscopic TLS source in these materials.

Superconducting qubits and SRF cavities both operate in a regime where microwave losses must be extraordinarily small, yet in practice their performance is often limited by dissipation and noise originating in the near-surface dielectric environment [1]. A leading source of this loss is attributed to ensembles of two-level systems (TLS) in the native oxides of commonly used superconducting metals—most notably Nb and Ta—which couple to electric fields and reduce qubit coherence times through dielectric loss and frequency noise, while limiting SRF cavity quality factors via residual and field-dependent dissipation [2, 3]. Identifying the microscopic origin of TLS in Nb and Ta oxides at microwave frequencies has therefore become a central materials challenge for the field, and a key bottleneck to improving both coherence and  $Q$  through rational materials design.

However, despite their importance, the microscopic physical mechanisms responsible for TLS in technologically relevant oxides remain unknown. Many distinct microscopic processes can generate similar experimental signatures—atomic tunneling between nearly degenerate configurations, molecular reorientations or rotor-like defects, charge trapping, or fine-structure splittings—so most evidence is indirect and correlation-based [1]. For Nb and Ta, several trends are repeatedly reported: TLS loss increases with the degree of amorphous disorder [4]; it is primarily associated with the pentoxide rather than more metallic suboxides (especially in Nb) [5]; it correlates with oxygen-vacancy content [2]; and Nb oxide appears measurably more lossy than Ta oxide (about 30% higher loss tangent) [6]. These observations constrain the space of mechanisms, but they do not uniquely identify the underlying microscopic origin.

In Nb and Ta oxides, prior work has often emphasized electronic defects—unpaired electrons and local magnetic moments in substoichiometric pentoxide [7], as well as dangling-bond–like centers—as plausible TLS origins [8]. However, while such electronic defects are plausible, the TLS landscape in amorphous oxides is likely broader, and atomic-scale tunneling mechanisms—particularly involving light impurities—have been less systematically

explored. Hydrogen is a strong candidate: it is readily incorporated into the oxide during oxidation and ambient exposure [2], is expected to interact strongly with oxygen-vacancy motifs [9], and—because of its small mass—could in principle undergo quantum motion among nearby configurations, potentially producing appreciable electric-dipole fluctuations. Consistent with this picture, studies on Al<sub>2</sub>O<sub>3</sub> and related dielectrics have highlighted H-based motifs as plausible TLS mechanisms [10–12]. Motivated by these considerations, we investigate hydrogen tunneling in amorphous Nb and Ta oxides using first-principles calculations accelerated by machine-learned interatomic potentials to sample realistic amorphous environments. Our results identify a set of candidate hydrogen-related two-level systems consistent with key experimental correlations and connect atomistic defect physics to measured loss trends in the  $\sim 0.1 - 10$  GHz microwave frequency range.

*Computational methods.* —

The amorphous nature of Nb<sub>2</sub>O<sub>5</sub> and Ta<sub>2</sub>O<sub>5</sub> makes symmetry-based identification of candidate interstitial sites for light atoms challenging, and realistic structural models are sufficiently large that brute-force DFT sampling is prohibitive. We therefore combine a modern machine-learning interatomic potential (MLIP) with targeted *ab initio* validation to map the interstitial landscape in bulk metal and oxide cells. Using the `fairchem` MLIP [13], we relax structures seeded from a uniform three-dimensional grid of trial interstitial positions with 1 Å spacing (smaller than the tetrahedral–tetrahedral separation in bulk Nb, 1.17 Å) inside each unit cell of either crystalline metal or previously generated amorphous oxide structures [7] (Fig. 1). The converged interstitial coordinates are clustered using a 0.1 Å cutoff to identify unique interstitial configurations, for which we record relaxed fractional coordinates and formation energies relative to the pristine host cell and molecular H<sub>2</sub>.

Candidate diffusion pathways were generated by connecting nearby unique sites. Minimum-energy paths and activation barriers were then obtained using the nudged elastic band (NEB) method [14]. All large-scale NEB cal-

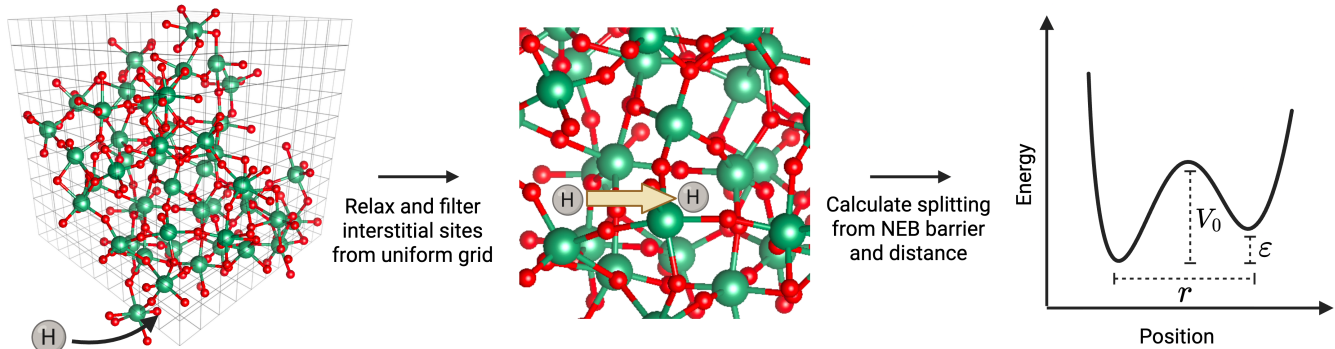


FIG. 1. Workflow for identifying hydrogen-related TLS in Nb and Ta pentoxide. (1) Place H on a uniform three-dimensional grid (1 Å spacing) and relax each seed to the nearest minimum; cluster the results to obtain unique interstitial sites. (2) Connect neighboring sites and compute minimum-energy paths and diffusion barriers using the NEB method. (3) For each hop, extract the site-to-site separation  $r$ , barrier height  $V_0$ , and estimate the tunnel splitting  $\Delta$  (and frequency  $f$ ) via the quartic WKB expression (Eq. (2)).

calculations used the `fairchem` MLIP, while a representative subset of interstitial endpoints and NEB barriers was validated with density-functional theory (DFT) using the open-source plane-wave code JDFTx [15, 16], employing ultrasoft pseudopotentials [17]. We used plane-wave cut-offs of 20 Hartree for the electronic wave functions and 100 Hartree for the electron density. Calculations employed the PBE exchange–correlation functional [18] and Monkhorst–Pack  $2 \times 2 \times 2$   $k$ -point meshes [19]. Bulk Nb was modeled using a  $4 \times 4 \times 4$  bcc supercell (64 atoms). For the amorphous oxides, we used a total of 49 distinct  $\text{Nb}_2\text{O}_5$  cells and 49 distinct  $\text{Ta}_2\text{O}_5$  cells, spanning seven oxygen-vacancy compositions and total sizes of 162–168 atoms, taken from Pritchard *et al.* [7]. These structures provide realistic amorphous oxide environments and a sufficiently large ensemble for robust statistics.

*Theoretical Background: WKB model for TLS tunneling.*— Microwave loss experiments are sensitive to defects with transition energies in the  $\mu\text{eV}$  range. Such splittings are far below what can be resolved directly from total-energy differences in first-principles calculations. We therefore use a semiclassical Wentzel–Kramers–Brillouin (WKB) approach, which relates the tunneling splitting to the *shape* of the underlying double-well potential—barrier height, curvature, and hop distance—quantities that are directly accessible from NEB minimum-energy paths.

A defect with two nearby configurations separated by a barrier can be mapped, at low temperatures, onto an effective two-level system (TLS) [1, 20, 21],

$$\hat{H}_{\text{TLS}} = \frac{1}{2} \varepsilon \sigma_z + \frac{1}{2} \Delta \sigma_x, \quad E_{01} = \sqrt{\Delta^2 + \varepsilon^2} = hf, \quad (1)$$

where  $\varepsilon$  is the energy asymmetry between the two minima and  $\Delta$  is the tunnel splitting.

To estimate  $\Delta$  from an NEB barrier, we approximate the minimum-energy path by an effective one-dimensional symmetric quartic double well characterized by a barrier height  $V_0$  and minimum-to-minimum separation  $r = 2a$ , and evaluate the splitting using a closed-form WKB approximation for a quartic potential [22],

$$\Delta = 4\sqrt{3} \hbar \omega \left( \frac{S_0}{2\pi\hbar} \right)^{1/2} e^{-S_0/\hbar}, \quad (2)$$

with  $\omega = (8V_0/ma^2)^{1/2}$  and  $S_0/\hbar = 16V_0/(3\hbar\omega)$ . In this Letter we use Eqs.(1) and (2) to identify candidate tunneling defects in the 0.1–10 GHz band, spanning the operating range of superconducting qubits and the low-GHz regime relevant to SRF cavities.

*Results and discussion.*—

We first benchmark the workflow in crystalline bcc Nb, which provides a well-defined reference for calibrating the tunneling model and connects directly to recent first-principles work on H in Nb [23]. We consider H, O, and N—species commonly present during processing and oxidation—and probe three representative local environments: pristine Nb, Nb with an interstitial O at an octahedral site, and Nb containing a niobium vacancy.

Figure 2 maps the NEB results in the  $(r, V_0)$  plane (the maximum along the minimum-energy path relative to the minima) for H, O, and N. The shaded band indicates the quartic-WKB isofrequency region corresponding to  $f = 0.1$ –10 GHz, computed from Eqs.(1) and (2) for geometrically symmetric sites with  $\varepsilon = 0$  using the tunneling mass of each species; dashed lines mark the 0.1 and 10 GHz boundaries. Points within this band correspond to tunnel splittings in the relevant microwave range, whereas points outside of it correspond to exponentially different splittings.

For hydrogen Fig. 2(a), the MLIP+NEB results cluster

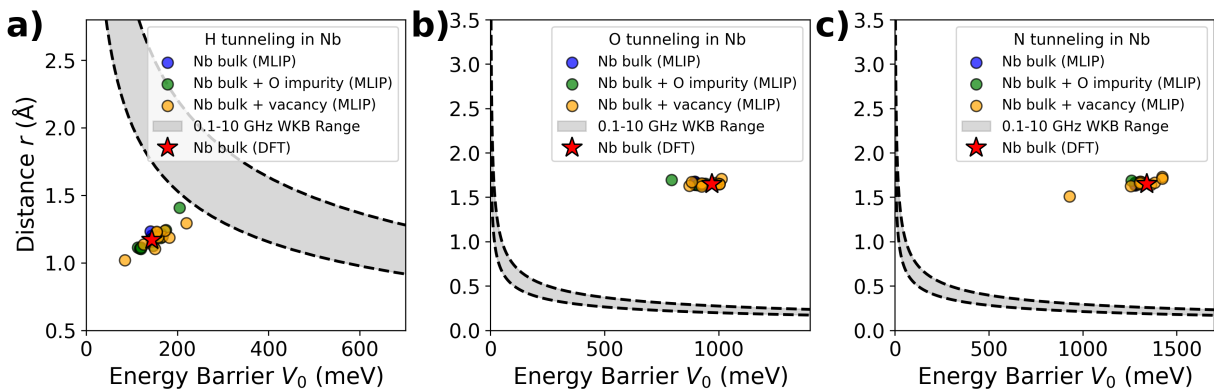


FIG. 2. Minimum-to-minimum distance  $r$  versus barrier height  $V_0$  for hops in bcc Nb, obtained from MLIP-based NEB, for (a) H, (b) O, and (c) N. Colors denote the local environment: pristine Nb (blue), Nb with an interstitial O at an octahedral site (green), and Nb with an Nb vacancy (yellow). A DFT cross-check for pristine Nb is indicated by a star. The shaded band (bounded by dashed lines) shows the quartic-WKB isofrequency region corresponding to  $f = 0.1\text{--}10$  GHz, computed using the tunneling mass of the diffusing species ( $m_H$ ,  $m_O$ ,  $m_N$ ). Points within the band yield microwave-scale tunnel splittings, whereas points well above it correspond to exponentially suppressed splittings.

around  $V_0 \approx 100\text{--}200$  meV and  $r \approx 1.17$  Å, consistent with the tetrahedral-tetrahedral separation. These hops lie near, but mostly just outside, the 0.1–10 GHz quartic-WKB window. A DFT cross-check (star) falls within the same cluster, supporting the use of MLIP-derived barriers and separations for broad searches and order-of-magnitude frequency estimates. Introducing a nearby O impurity or an Nb vacancy perturbs  $V_0$  and  $r$  only modestly (by tens of meV and a few hundredths of an Å), shifting the inferred  $\Delta$  but not enough to bring these hops into the 0.1–10 GHz window.

In contrast, oxygen and nitrogen hops Figs. 2(b,c) lie far from the TLS-relevant region: barriers of  $V_0 \sim 0.8\text{--}1.5$  eV with  $r \sim 1.65$  Å (octahedral-octahedral separation) place them well outside the 0.1–10 GHz WKB band for their larger tunneling masses, implying splittings  $\ll 0.1$  GHz. Thus O and N interstitials are unlikely to be the primary intrinsic TLS in bulk Nb. They can nevertheless reshape the hydrogen landscape (e.g., by trapping or biasing nearby sites), and thereby influence H-based tunneling indirectly.

Overall, interstitials heavier than H would require unrealistically small separations ( $\lesssim 0.5$  Å) to reach the microwave WKB band, and in practice they also tend to exhibit larger barriers. Hydrogen is therefore the only plausible light interstitial in Nb with barrier-distance combinations near the relevant microwave TLS window, motivating our focus on H-related defects in the oxide.

We next turn to amorphous  $M_2O_{5-\delta}$  ( $M=\text{Nb,Ta}$ ). Using seven independent realizations obtained from [7] at each of seven oxygen-deficiency levels spanning  $0 \leq \delta \leq 0.250$ , we sampled the H interstitial landscape in both oxides. Our pipeline of grid seeding, local relaxation, and clustering yielded 9,787 and 9,327 distinct relaxed H minima in  $\text{Nb}_2\text{O}_{5-\delta}$  and  $\text{Ta}_2\text{O}_{5-\delta}$ , respectively. Fig. 3 shows that increasing oxygen deficiency stabilizes H in both oxides, shifting the formation-energy distributions

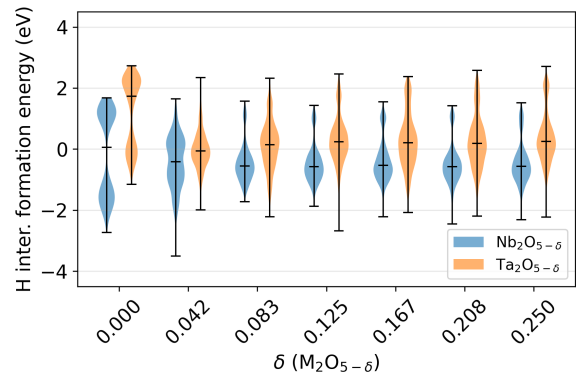


FIG. 3. Distribution of H interstitial formation energies over the set of distinct relaxed interstitial sites identified in each amorphous cell (median and interquartile range shown in black) as a function of the oxygen vacancy composition  $\delta$ .

to lower values. At every  $\delta$ ,  $\text{Nb}_2\text{O}_{5-\delta}$  exhibits systematically lower H formation energies than  $\text{Ta}_2\text{O}_{5-\delta}$ , indicating a stronger thermodynamic tendency for H incorporation in Nb pentoxide, consistent with observations [4].

The key quantity in TLS physics is not the behavior of any individual defect but the statistical distribution of TLS parameters [24]. We therefore consider all distinct pairs of relaxed H interstitial sites with minima energy asymmetry  $\varepsilon \leq 10$  meV and separation  $r \leq 1.65$  Å, and compute the corresponding MLIP-NEB barriers. For each pair, Eq.2 gives the tunnel splitting  $\Delta$ , while the endpoint energy difference defines the asymmetry  $\varepsilon$ . Fig. 4 shows the resulting distributions. Since  $\Delta$  depends exponentially on the action  $S_0$  and spans many orders of magnitude, we fit  $\log(\Delta)$  with a Gaussian-mixture model, a representation consistent with the approximately log-

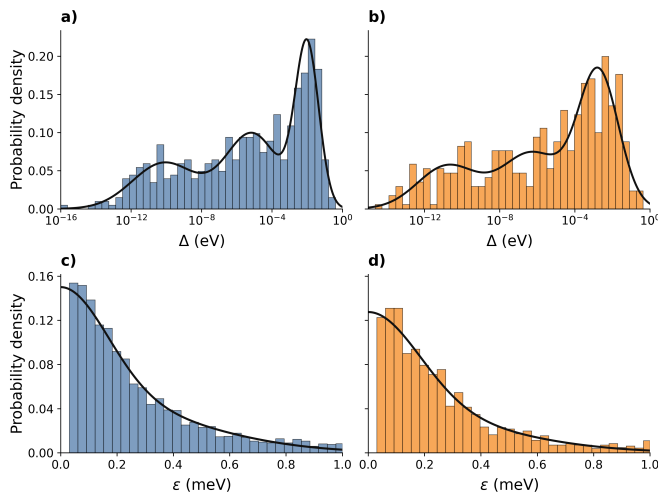


FIG. 4. Statistical distributions of hydrogen TLS parameters in amorphous  $\text{Nb}_2\text{O}_{5-\delta}$  and  $\text{Ta}_2\text{O}_{5-\delta}$ . (a,b) Probability density of tunnel splittings  $\Delta$  for all distinct pairs of relaxed H minima with endpoint energy difference  $\leq 10$  meV and separation  $\leq 1.65$  Å. Solid curves show Gaussian-mixture fits to  $\log(\Delta)$ . (c,d) Probability density of asymmetries  $\varepsilon$  for the same pair ensemble. Because endpoint energy differences below 0.05 meV are not reliably resolved in the MLIP total energies, the solid curves show grouped two-component half-normal-mixture fits used to extrapolate the low- $\varepsilon$  tail relevant to TLS statistics.

uniform ( $1/\Delta$ ) distributions often assumed in statistical TLS models. For  $\varepsilon$ , however, the TLS-relevant low-asymmetry tail lies below the direct numerical resolution of the MLIP energies. The 0.1–10 GHz TLS window corresponds to  $\varepsilon \lesssim 0.05$  meV, and smaller endpoint differences cannot be resolved reliably within the numerical limitations of the MLIP energies. We therefore model the resolved  $\varepsilon$  distribution with a grouped two-component half-normal mixture and use it to extrapolate the sub-0.05 meV regime entering the statistical TLS estimate.

To connect the atomistic pair statistics to an effective TLS density, we construct a simple ensemble model based on the fitted  $\Delta$  and  $\varepsilon$  distributions. For each oxide, let  $n_{\text{site}}$  denote the density of distinct relaxed H interstitial sites and  $z_{\text{eff}}$  the mean number of neighboring minima within the 1.65 Å cutoff. The density of distinct candidate pairs is then  $\frac{1}{2}n_{\text{site}}z_{\text{eff}}$  where the factor 1/2 removes double counting. If the H occupation per interstitial site is  $x_{\text{site}}$ , the probability that a pair hosts exactly the one H atom required for a tunneling defect is  $2x_{\text{site}}(1-x_{\text{site}})$ . Next, we estimate the probability  $p_{\text{avg}}$  that such an occupied pair lies in the microwave TLS window by introducing the joint distribution of tunneling splitting  $\Delta$  and asymmetry  $\varepsilon$ ,

$$\begin{aligned} P(\Delta, \varepsilon) &= P(\Delta|\varepsilon)P(\varepsilon) \\ &\approx P(\Delta||\varepsilon| < 10 \text{ meV})P(\varepsilon) \\ &\equiv p_{\Delta}(\Delta)p_{\varepsilon}(\varepsilon), \end{aligned}$$

where we assume that for asymmetries  $|\varepsilon| < 10$  meV the

asymmetry has negligible influence on the statistics of the barrier height and tunneling distance, and hence on the tunneling splitting  $\Delta$ . Integrating  $P(\Delta, \varepsilon)$  over the semi-annular region in  $(\Delta, \varepsilon)$  space corresponding, via Eq. (1), to TLS frequencies in the microwave band then yields  $p_{\text{avg}}$ .

The resulting TLS density is

$$\rho_{\text{eff}} = \left(\frac{1}{2}n_{\text{site}}z_{\text{eff}}\right) [2x_{\text{site}}(1-x_{\text{site}})] p_{\text{avg}}. \quad (3)$$

Finally, we convert  $\rho_{\text{eff}}$  into an intrinsic low-field dielectric loss using the standard TLS expression [25]

$$\tan \delta_0 = \frac{\pi \rho_{\text{eff}} p^2}{3 \varepsilon_r \varepsilon_0}, \quad (4)$$

where  $p$  is a representative dipole moment for the H hop and  $\varepsilon_r$  is the dielectric constant of the oxide.

We estimate the TLS-relevant dipole change  $\Delta \mathbf{p}$  between endpoint minima from Bader charges [26], obtaining a mean magnitude  $|\Delta \mathbf{p}| \approx 1.1$  D in both oxides. This Debye-scale dipole change is consistent with values commonly inferred for TLS in amorphous dielectrics and junction barriers [27], implying appreciable coupling to microwave electric fields. With  $p \approx |\Delta \mathbf{p}|$ , we evaluate Eq. (4) using dielectric constants  $\varepsilon_r = 45$  for  $\text{Nb}_2\text{O}_5$ , consistent with Ref. [5], and  $\varepsilon_r = 21$  for  $\text{Ta}_2\text{O}_5$ , representative of reported amorphous-film values [28, 29]. The only remaining external parameter we need is then the hydrogen concentration, which sets the site occupation factor  $x_{\text{site}}$ . We therefore evaluate  $\rho_{\text{eff}}$  over a physically reasonable range of H contents, 1–3 at.%, motivated by reported experimental observations of hydrogen incorporation in Nb and Ta oxides [30, 31].

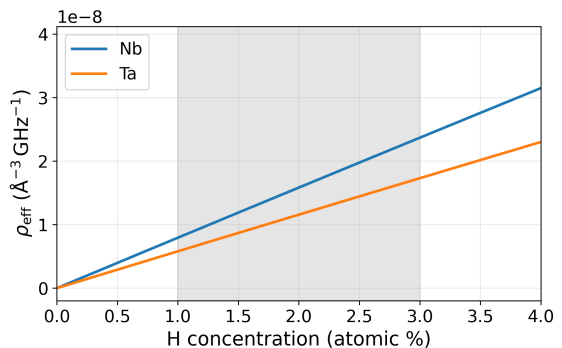


FIG. 5. Effective TLS density  $\rho_{\text{eff}}$  in amorphous  $\text{Nb}_2\text{O}_{5-\delta}$  and  $\text{Ta}_2\text{O}_{5-\delta}$  as a function of hydrogen concentration, obtained from the statistical pair model described in the text. The larger  $\rho_{\text{eff}}$  predicted for Nb reflects the higher probability of microwave-active H tunneling defects extracted from the atomistically derived pair statistics. The shaded region marks the physically relevant H-concentration range considered in this work.

The resulting curves, shown in Fig. 5, place the predicted effective TLS density  $\rho_{\text{eff}}$  in the experimentally

relevant range and naturally predict a larger TLS population in  $\text{Nb}_2\text{O}_{5-\delta}$  than in  $\text{Ta}_2\text{O}_{5-\delta}$ . This difference originates from the atomistically derived pair statistics, which give a higher probability of microwave-active H tunneling defects in Nb. Using these  $\rho_{\text{eff}}$  values in Eq. (4), we obtain for  $\text{Nb}_2\text{O}_{5-\delta}$  at  $\sim 2$  at.% H a loss estimate of  $\tan \delta_0 \approx 8.6 \times 10^{-4}$ , within the experimentally reported Nb pentoxide range of  $8.1 \times 10^{-4}$  to  $1.8 \times 10^{-3}$  [5]. For  $\text{Ta}_2\text{O}_{5-\delta}$ , we instead use a lower H concentration of  $\sim 1$  at.%, motivated by our results and by the experimental evidence for reduced hydrogen incorporation in Ta oxide [4]. The resulting smaller  $\tan \delta_0 \approx 6.7 \times 10^{-4}$  leads to a correspondingly lower loss estimate, consistent with the observed trend that Ta oxides are roughly 30% less lossy than Nb oxides [6].

The workflow introduced here is not specific to  $\text{Nb}_2\text{O}_{5-\delta}$  and  $\text{Ta}_2\text{O}_{5-\delta}$ . By analyzing amorphous structures, identifying nearby minima connected by diffusion pathways, and extracting descriptors relevant to tunneling and dipole coupling, it provides a transferable framework for screening double-well motifs compatible with microwave TLS behavior. The same strategy can be applied to other disordered dielectrics, oxide interfaces, and tunnel-barrier materials used in superconducting devices, where light impurities and defect complexes are often expected. More broadly, this perspective shifts the discus-

sion from isolated “candidate TLS” examples to defect ensembles that can be compared quantitatively across materials.

*Conclusions.* — We have combined MLIP-accelerated exploration of hydrogen configurations in amorphous oxides with targeted *ab initio* validation to identify hydrogen tunneling as a plausible microscopic origin of TLS in  $\text{Nb}_2\text{O}_{5-\delta}$  and  $\text{Ta}_2\text{O}_{5-\delta}$ . In bulk Nb, H is the only interstitial species among H, O, and N with barrier–distance combinations near the microwave tunneling regime. In the amorphous pentoxides, statistical sampling of nearby H minima yields distributions of tunnel splittings and asymmetries that can be coarse-grained into an effective TLS density and intrinsic loss estimate. The model predicts  $\tan \delta_0 \approx 8.6 \times 10^{-4}$  for  $\text{Nb}_2\text{O}_{5-\delta}$  at  $\sim 2$  at.% H and  $\tan \delta_0 \approx 6.7 \times 10^{-4}$  for  $\text{Ta}_2\text{O}_{5-\delta}$  at  $\sim 1$  at.% H, consistent with the observed trend of lower loss in Ta oxide. More broadly, the approach introduced here offers a transferable route for screening TLS-active motifs in disordered dielectrics and interfaces relevant to superconducting devices.

*Acknowledgements.* — We thank Nathan Sitaraman for useful feedback and discussions.

This work was supported by the US National Science Foundation under award PHY-1549132, the Center for Bright Beams.

- 
- [1] C. Müller, J. H. Cole and J. Lisenfeld, *Reports on Progress in Physics* **82** 124501 (2019).
- [2] D. Bafia, M. R. Vissers and D. P. Pappas, *Physical Review Applied* **22** 024035 (2024).
- [3] M. Wenskat, D. Reschke, M. Schilling et al., *Physical Review B* **106** 094516 (2022).
- [4] J.-S. Oh, R. Zaman, A. A. Murthy, M. Bal, F. Crisa, S. Zhu, C. G. Torres-Castanedo, C. J. Kopas, J. Y. Mutus, D. Jing et al., *ACS nano* **18** 19732–19741 (2024).
- [5] V. Ganesan, J. Zhang, D. G. Wild and A. Bezryadin, (2026).
- [6] D. P. Goronzy, W. W. Mah, P. G. Lim, T. Guess, S. Majumder, D. A. Garcia-Wetten, M. J. Walker, J. Ramirez, W.-R. Syong, D. Bennett et al., (2025).
- [7] P. G. Pritchard and J. M. Rondinelli, *Physical Review Applied* **23** 064062 (2025).
- [8] Z. Wang, C. C. Yu and R. Wu, *Physical Review Applied* **23** 024017 (2025).
- [9] X. Peng, S. Zhang, Z. Bao, L. Ding, G. Wang, Y. Shao, Z. Xu, W. Ji, G. Feng, S. Wang et al., *Chemical Communications* **58** 8428–8431 (2022).
- [10] M. S. Khalil, M. J. A. Stoutimore, F. C. Wellstood and K. D. Osborn, *Applied Physics Letters* **103** 162601 (2013).
- [11] L. Gordon, A. Janotti and C. G. Van de Walle, *Scientific Reports* **4** 7590 (2014).
- [12] S. Mittal, K. Adachi, N. E. Frattini, M. D. Urmey, S.-X. Lin, A. L. Emser, C. Metzger, L. Talamo, S. Dickson, D. Carlson et al., *Physical Review Applied* **21** 054044 (2024).
- [13] FAIR Chemistry, fairchem: FAIR chemistry’s library of machine learning methods for chemistry (2025), accessed 2025-10-22.
- [14] H. Jónsson, G. Mills and K. W. Jacobsen, Nudged elastic band method for finding minimum energy paths of transitions, In *Classical and Quantum Dynamics in Condensed Phase Simulations* 385–404 World Scientific (1998).
- [15] M. C. Payne, M. P. Teter, D. C. Allan, T. Arias and a. J. Joannopoulos, *Reviews of modern physics* **64** 1045 (1992).
- [16] R. Sundararaman, K. Letchworth-Weaver, K. A. Schwarz, D. Gunceler, Y. Ozhobes and T. Arias, *SoftwareX* **6** 278–284 (2017).
- [17] K. F. Garrity, J. W. Bennett, K. M. Rabe and D. Vanderbilt, *Computational Materials Science* **81** 446–452 (2014).
- [18] J. P. Perdew, K. Burke and M. Ernzerhof, *Physical Review Letters* **77** 3865–3868 (1996).
- [19] H. J. Monkhorst and J. D. Pack, *Physical Review B* **13** 5188–5192 (1976).
- [20] P. W. Anderson, B. I. Halperin and C. M. Varma, *Philosophical Magazine* **25** 1–9 (1972).
- [21] W. A. Phillips, *Journal of Low Temperature Physics* **7** 351–360 (1972).
- [22] A. Garg, *American Journal of Physics* **68** 430–437 (2000).
- [23] N. Abogoda, D. A. Papaconstantopoulos and H. Wipf, *Physical Review B* **111** L020103 (2025).
- [24] W. A. Phillips, *Reports on Progress in Physics* **50** 1657–1708 (1987).
- [25] J. M. Martinis, K. B. Cooper, R. McDermott, M. Steffen, M. Ansmann, K. Osborn, K. Cicak, S. Oh, D. P. Pappas,

- R. W. Simmonds et al., *Physical review letters* **95** 210503 (2005).
- [26] G. Henkelman, A. Arnaldsson and H. Jónsson, *Computational Materials Science* **36** 354–360 (2006).
- [27] J. Lisenfeld, A. Bilmes, A. Megrant, R. Barends, J. Kelly, P. Klimov, G. Weiss, J. M. Martinis and A. V. Ustinov, *npj Quantum Information* **5** 105 (2019).
- [28] K. Chen, M. Nielsen, G. Yang, E. Rymaszewski and T.-M. Lu, *Journal of electronic materials* **26** 397–401 (1997).
- [29] G. Sethi, M. Olszta, J. Li, J. Sloppy, M. W. Horn, E. C. Dickey and M. T. Lanagan, Structure and dielectric properties of amorphous tantalum pentoxide thin film capacitors (2007), In *2007 Annual Report Conference on Electrical Insulation and Dielectric Phenomena*, pp. 815–818. IEEE.
- [30] S. B. Basuvalingam, B. Macco, H. Knoops, J. Melskens, W. M. Kessels and A. A. Bol, *Journal of Vacuum Science & Technology A* **36** (2018).
- [31] M. Molina-Ruiz, K. Shukla, A. Ananyeva, G. Vajente, M. Abernathy, T. Metcalf, X. Liu, A. Markosyan, R. Bassiri, M. Fejer et al., *Physical Review Materials* **8** 035603 (2024).